Supporting Material

for "Coupled Flexibility Change in Cytochrome P450cam Substrate Binding Determined by Neutron Scattering, NMR and Molecular Dynamics Simulation" by Yinglong Miao, Zheng Yi, Carey Cantrell, Dennis Glass, Jerome Baudry, Nitin Jain and Jeremy C. Smith.

I. Experiments

I.1 Sample Preparation

Expression and purification of camphor-bound CYP101 followed methods described previously(1). The substrate-free sample was prepared by extensive dialysis of camphor-bound protein with multiple buffer exchanges using substrate-free buffer (50 mM potassium phosphate, 50 mM KCl, pH 7.4), followed by gel filtration chromatography to ensure complete removal of the camphor. The samples were then checked via UV-VIS spectroscopy to confirm removal of substrate by monitoring the Soret absorption maximum at 418 nm which corresponds to the low-spin, water-coordinated substrate-free form. Substrate-free and camphor-bound ^{15}N, ^{2}H (70% ^{2}H) samples of CYP101 (~0.3-0.5 mM concentration) were prepared and used for NMR relaxation and NOE experiments described below. A ^{13}C, ^{15}N, ^{2}H (70% ^{2}H) triple-labeled sample was also prepared in substrate-free form as described above and used for triple resonance backbone assignment experiments.

For the neutron scattering experiments, the protein samples (~200 mg) were repeatedly dissolved in the CYP101 camphor-bound and substrate-free buffers prepared with 99.99% D_2O to replace the exchangeable hydrogen atoms with deuterium, and then lyophilized. The dried protein samples were hydrated to $h \approx 0.4$g D_2O/g protein at room temperature by exposing the protein samples to D_2O vapor in a closed desiccator. The buffer concentrations were adjusted prior to lyophilization and hydration to achieve an effective concentration of buffer similar to those used for the NMR experiments. A small portion of each sample was redissolved in

CYP101 camphor-bound and substrate-free buffers to check for stability and confirm the spin-state of the protein by UV-VIS spectroscopy. The sample hydration levels were determined from the mass change during hydration. The masses of the samples were measured before and after neutron scattering experiments and no change was detected. The protein masses and hydration levels of the final prepared samples are listed in Table S1a. The hydrated powder samples were packed in aluminum foil (3cm x 10cm) and sealed in annular sample cans for the neutron scattering measurements.

Table S1 (a) Substrate-free and camphor-bound CYP101 samples prepared for neutron scattering experiments and (b) detailed instrumental parameters including the q range, energy resolution and energy range for the three neutron scattering instruments used.

Sample	**Protein mass (mg)**	***h* (g water/g protein)**
H(substrate-free CYP101) + D_2O	182.1	0.39
H(camphor-bound CYP101) + D_2O	183.3	0.37

(a)

Instrument	**HFBS**	**BASIS**	**CNCS**
q ($Å^{-1}$)	[0.25, 1.75]	[0.30, 1.90]	[0.04, 2.00]
E (μeV)	[-17.2, 17.2]	[-119.8, 119.8]	[-1600,1600]
Resolution (μeV)	1	3.5	25

(b)

I.2 Quasielastic Neutron Scattering

Quasielastic neutron scattering spectra were collected for the hydrated substrate-free and camphor-bound CYP101 samples at T=300K on the NG2 high-flux backscattering spectrometer (HFBS) at the Center for Neutron Research at National Institute of Standard and Technology (NIST), and the Backscattering Spectrometer (BASIS)(2) and Cold Neutron Chopper Spectrometer (CNCS)(3) at the Spallation Neutron Source (SNS) at Oak Ridge National Laboratory (ORNL). These three spectrometers together cover a broad energy range, from 1 μeV to 1.6 meV. The data collection times for each measurement were ~8 hours on HFBS, ~10 hours on BASIS and ~4 hours on CNCS. Detailed instrumental parameters including the space vector q

range, energy resolution and energy range are listed in Table S1b. No correction for multiple scattering was applied since the neutron transmission was over 0.9 and multiple scattering is thus negligible. The experimental neutron scattering data were reduced and analyzed using the program DAVE(4) provided by the NIST Center for Neutron Research (NCNR).

I.3 NMR Spin Relaxation Experiments

^{1}H-^{15}N backbone assignments for camphor-bound CYP101 have been published previously (1) and were used directly for order parameter analysis. Backbone assignments for substrate-free CYP101 were resolved via a set of 3D [^{15}N,^{1}H]-TROSY-HNCA, [^{15}N,^{1}H]-TROSY-HN(CO)CA and [^{15}N,^{1}H]-TROSY-HNCO experiments (5-6) acquired on a triply-labeled ^{13}C,^{15}N,^{2}H sample. While assignments for 100 residues were available for camphor-bound CYP101, resonance overlap/line-broadening enabled assignments for only 92 residues for substrate-free CYP101. All acquired NMR data were processed and analyzed using FELIX (Accelrys Inc, San Deigo CA), SPARKY and/or NMRPipe software (7).

NMR ^{15}N T_1, T_2 and ^{15}N-{^{1}H} NOE measurements were recorded on both substrate-free and camphor-bound samples of CYP101 using 2D ^{1}H-^{15}N HSQC experiments with water suppression (8). T_1 measurements were accomplished using variable relaxation delays of 0, 60, 160, 240, 400, 800 and 1200 ms, with duplicate measurement at 240 ms for error estimation. T_2 experiments were similarly performed using relaxation delays of 10, 30, 50, 70 and 90 ms along with a duplicate measurement at 50 ms for error estimation. A recycle delay of 3.5 s and 1.5 s was used for the T_1 and T_2 experiments, respectively. Extraction of T_1 and T_2 values from the peak intensity measurements was carried out by nonlinear least-squares fitting of the intensity changes to a single-exponential decay function. A set of NOE experiments, with and without

saturation, was recorded for measuring ^{15}N-{^{1}H} NOEs. A 5 s saturation/recovery period was used in the saturation experiment with an equivalent recovery time in the non-saturation experiment. As pointed out recently by Bax and coworkers (9), long saturation/recovery periods in conjunction with HSQC-based readout sequences help in reducing systematic errors in NOE measurements in highly deuterated proteins.

Internal mobility analysis of the relaxation and NOE data was performed with TENSOR_V2 software using the model selection criterion as outlined by Palmer and coworkers (10). T_1/T_2 values of 21 residues found in various secondary structure elements in CYP101 exhibiting minimal line-broadening in NMR spectra were used to initially estimate the overall rotational correlation time (*ca.* $\tau_c \sim 19$ ns). The rotational diffusion tensor was also estimated from corresponding T_1/T_2 values for both forms and found to be similar with the principal components in the ratio of 1: 0.7: 0.6, which corresponds close to an axially symmetric tensor. Model-free analysis proceeded further using the estimated tensor. Five sets of model-free parameters were fitted to the experimental T_1, T_2 and NOE data corresponding to the following models - Model 1: S^2_s, Model 2: S^2_s and τ_e, Model 3: S^2_s and R_{ex}, Model 4: S^2_s, τ_e and R_{ex}, Model 5: S^2_f, S^2_s and τ_e. In the models, S^2_s and S^2_f correspond to squares of order parameters for internal motions on the slow and fast time scales with the square of generalized order parameter $S^2 = S^2_s S^2_f$, τ_e is the effective correlation time for internal motions and R_{ex} accounts for chemical exchange. Data for each residue was fit progressively to the models for selection of appropriate model and optimization of internal mobility parameters. 200 cycles of Monte Carlo simulations were performed to determine the goodness-of-fit (within a 95% confidence limit) between the various models and experimental data. The above procedure led to the selection of Model 1 for 43 % of residues, Model 2 for 14 % of residues, Model 3 for 21 % of residues, Model 4 for 18 % of

residues and Model 5 for 4 % of residues in camphor-bound CYP101. For substrate-free CYP101, Model 1 was selected for 20 % of residues, Model 2 for 5 % of residues, Model 3 for 32 % of residues, Model 4 for 40 % of residues and Model 5 for 3 % of residues. In addition, while only 30 % of residues showed chemical exchange contributions in camphor-bound CYP101, about twice that number (~ 65 %) showed chemical exchange contributions in substrate-free CYP101. This is not surprising as substrate-free CYP101 is conformationally more mobile than the camphor-bound form as indicated by our MD simulations.

II. Simulations

Molecular dynamics simulation of substrate-free CYP101 was carried out using the 3L61 X-ray crystal structure that was solved at 1.5 Å resolution(11) . Residues 1 to 9 (N-terminus) and 90-97 (B' helix), 104 (one in B-C loop) are missing from the 3L61 crystal structure. The N-terminus was added as a random coil using the program MOE(12) with energy minimization applied. The initial coordinates of residues 90-97 and 104 were obtained from the 1PHC structure of substrate-free CYP101 after superimposing the rest of the protein backbone. The 3L63 crystal structure (1.5 Å resolution)(11) was used for simulating substrate-bound CYP101. The nine N-terminal residues also missing in 3L63 were added following the above procedure.

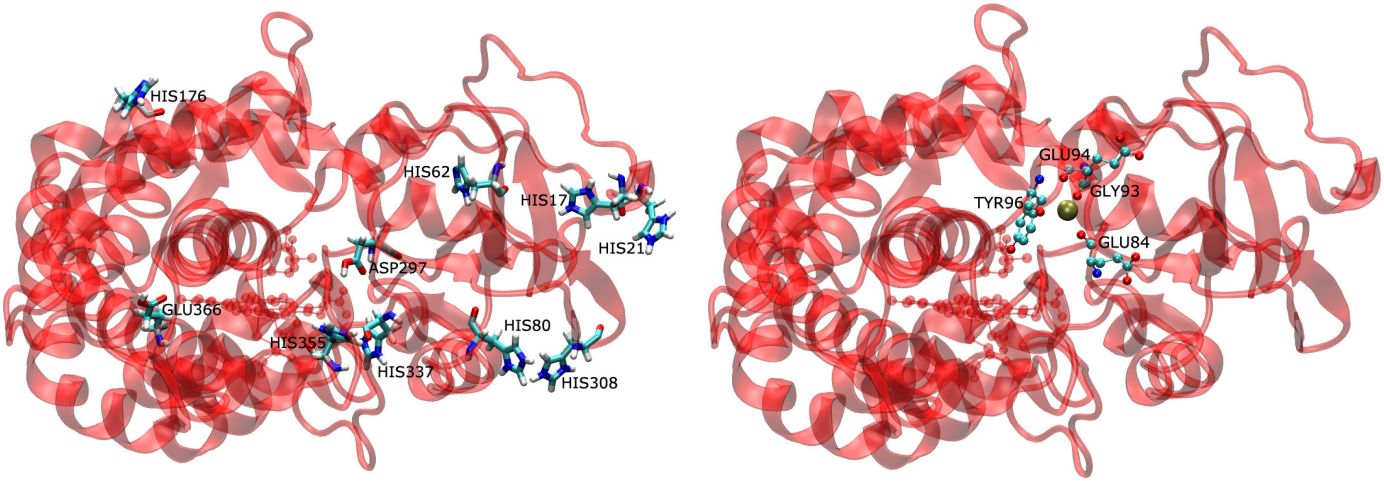

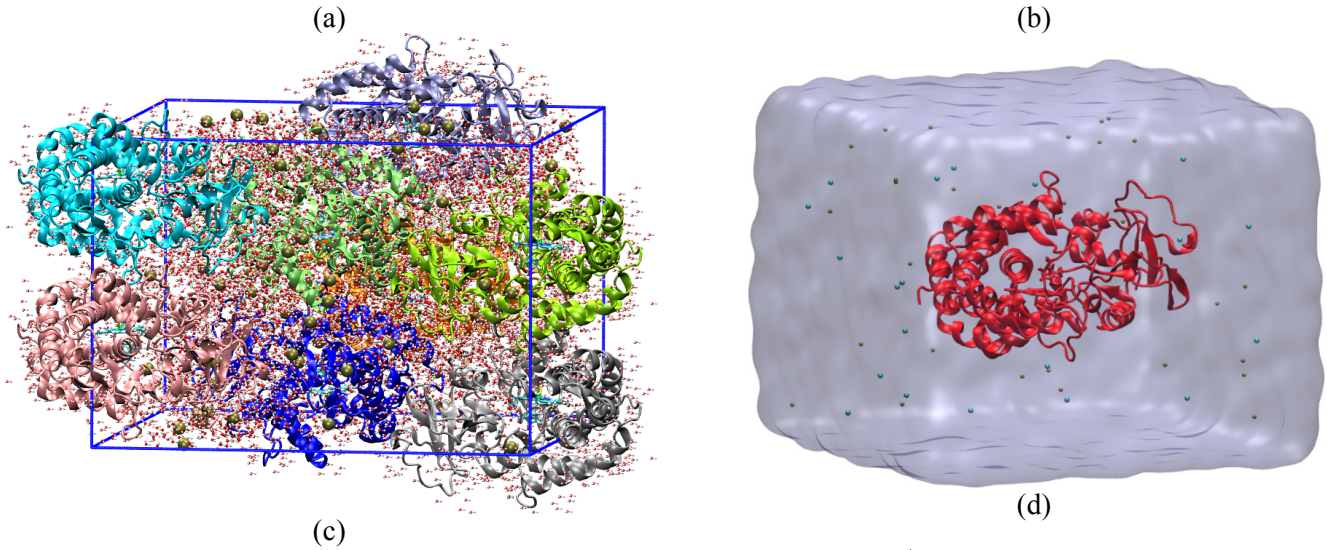

Fig. S1 (a) Residues with nonstandard protonation states and (b) K^+ binding site in camphor-bound CYP101 that is composed of backbone carbonyl oxygens of Glu84, Gly93, Glu94 and Tyr96. Schematic representations of (c) hydrated protein powder at h=0.4 g D_2O/g protein and (d) protein solvated in aqueous solution used in MD simulation.

The protonation states of protein residues follow the scheme described previously (13-14) with non-standard protonation applied for the following residues: Asp297 and Glu366 are protonated, His62 is protonated on δ-nitrogen, and seven other histidines (17, 21, 80, 176, 308, 337 and 355) are doubly protonated (Fig. S1a). A K^+ ion located at the cation binding site (composed of backbone carbonyl oxygens of Glu84, Gly93, Glu94 and Tyr96) as resolved in the 3L63 crystal was kept in the simulation (13-14) (Fig. S1b). The heme iron was coordinated to the sulfur atom of Cys357 in the active site, providing a five-coordinate high-spin state in camphor-bound CYP101, while in substrate-free CYP101 it was also coordinated to the oxygen atom of crystallographic water 541 forming a six-coordinated low-spin state (16-18).

For simulating CYP101 in hydrated powder form, a unit cell containing 4 proteins and the crystallographically-identified water molecules was constructed by applying transformation matrices provided in the PDB entries for both 3L61 substrate-free CYP101 and 3L63 camphor-bound CYP101(19), and replicated in the Z direction to generate an “a x b x 2c” lattice. A water

box was then overlaid on the protein lattice with all but the crystallographic water molecules and the additional required number of water molecules closest to the protein removed to yield a hydration level h=0.4 g water/g protein. There were 3,256 crystallographic water molecules in substrate-free CYP101 and 3,616 molecules in camphor-bound CYP101. 4,349 and 4,014 additional water molecules were added to substrate-free CYP101 and camphor-bound CYP101 respectively. The protein charges were neutralized using 0.1M KCl. The final system model of simulating CYP101 hydrated powder is shown in Fig. S1c.

For MD simulations of CYP101 in aqueous solution, each of the complete 3L61 and 3L63 structures was solvated in a rectangular box of TIP3P water molecules(20) extending at least 10 Å from the protein surface to the edge of the box with the crystallographically-identified water molecules kept by using the *solvate* plugin in VMD(21). K^+ and Cl^- ions were added at random locations in the bulk solvent to neutralize the system, achieving an ionic strength of 0.1 M using the *autoionize* plugin in VMD(21). A schematic representation of the resulting model system is shown in Fig. S1d. The final systems contain 49,791 atoms (14,386 water molecules) for substrate-free CYP101 and 46,568 atoms (13,305 water molecules) for camphor-bound CYP101.

MD simulations of substrate-free and camphor-bound CYP101 were performed by using NAMD2(22). Periodic boundary conditions were applied to CYP101 in both hydrated powder (Fig. S1c) and aqueous solution (Fig. S1d). The CHARMM22 force field(23) was used for the protein and the TIP3P model (20) for water molecules. Standard CHARMM force field parameters(23) were used for the heme group including an explicit Fe-S bond to Cys357, except that the atomic partial charge of the SG atom in Cys357 was adjusted to -0.07e to account for the resting state of CYP101 in both substrate-free and camphor-bound forms(13, 15). CHARMM parameters for camphor were obtained from Ref. (24). A cutoff distance of 12 Å was used for the

van der Waals and short-range electrostatic interactions and the long-range electrostatic interactions were computed with the particle-mesh Ewald summation method(25) using a grid point density of 1/Å. The SHAKE(26) algorithm was applied to all hydrogen-containing bonds. The systems were initially energy minimized with original atoms in the crystal structure fixed for 1000 steps to equilibrate the newly-added residues (notably the N-terminus), followed by another 1000 steps with all atoms free using the conjugate gradient algorithm. The systems were then gradually heated to 300 K at a rate of 60 K/ps and equilibrated at 300 K for 5 ns in constant volume (i.e, NVT ensemble) with atoms identified in the crystal structure fixed. The systems were further equilibrated in the NPT ensemble (300 K and 1 atm) with all atoms unconstrained lasting 100 ns for the CYP101 simulations in hydrated powder and 200 ns for the simulations in aqueous solution, and an additional 100 ns NPT production run was performed for all CYP101 simulations. A 2 fs integration time-step was used and a multiple-time-stepping algorithm(22) was employed with bonded and short-range nonbonded interactions computed every time-step and long-range electrostatic interactions every two time-steps.

III. Analysis

III.1 Quasielastic Neutron Scattering Spectra

Neutron dynamic structure factors, $S(q,\omega)$ of substrate-free and camphor-bound CYP101 measured at 300 K on the three neutron scattering instruments (HFBS, BASIS and CNCS) are shown in Figs. S2 (a), (b) and (c), respectively. Each dynamic structure factor was summed over all detectors with an average q of 1.0 $Å^{-1}$ for HFBS and CNCS and 0.9$Å^{-1}$ for BASIS, and the elastic peak was normalized to a vanadium standard.

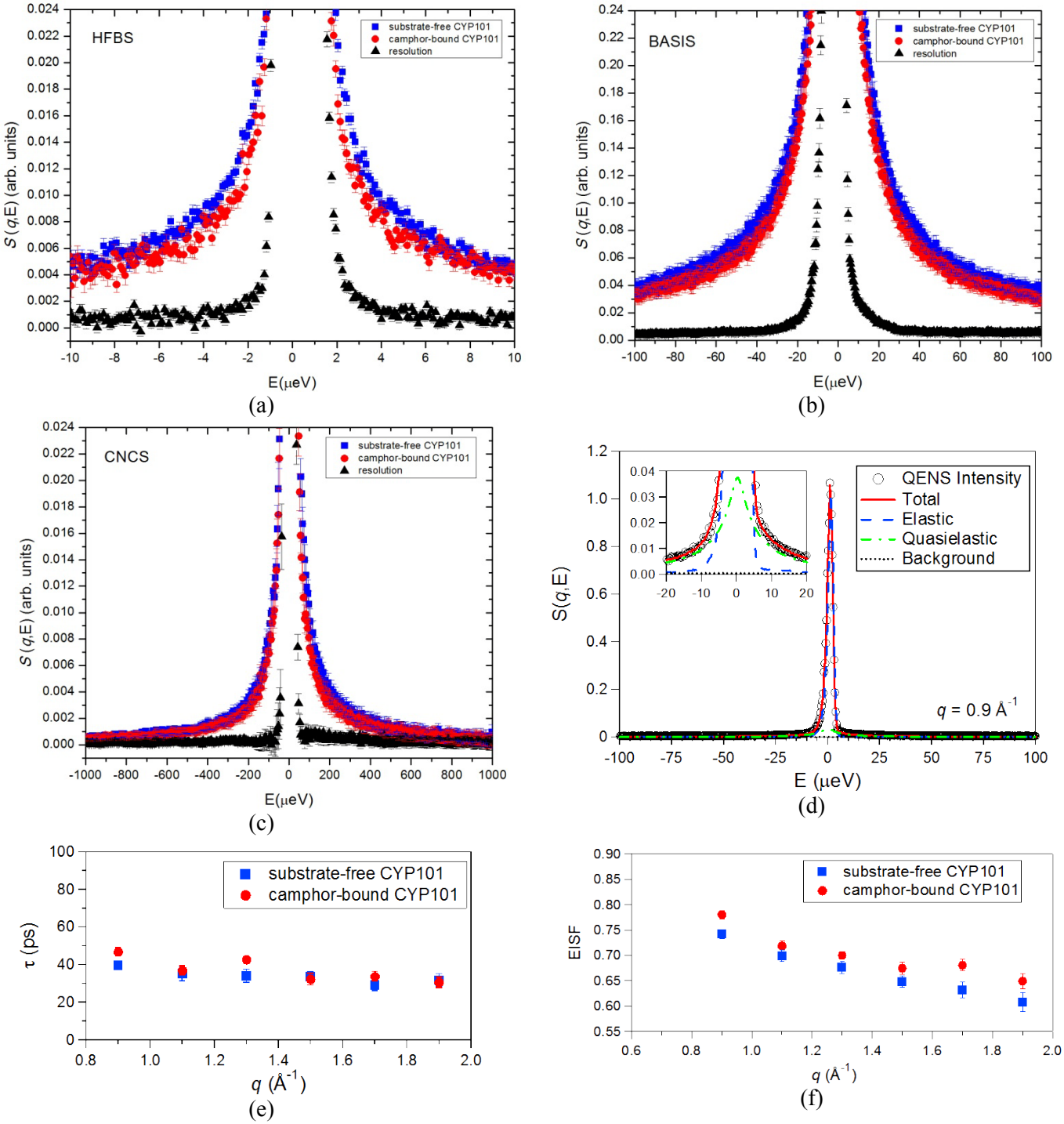

Fig. S2 Dynamic structure factors of substrate-free vs. camphor-bound CYP101 measured at 300K on (a) HFBS, (b) BASIS, and (c) CNCS. (d) Example fit of Eq. (S1) to $S(\boldsymbol{q},\omega)$ for substrate-free CYP101 measured on BASIS at q = 0.9Å^{-1}: hollow circles are the measured neutron intensity; solid red line is the fitted curve; black dotted, green dot-dashed, and blue dashed lines represent the background, quasielastic scattering (KWW function), and elastic scattering (δ-function), respectively. Plots of the resulting (e) protein relaxation time τ and (f) EISF.

To characterize the protein relaxation processes involved, $S(q,\omega)$ was fitted by the sum of a δ-function and a Kohlrausch-Williams-Watts (KWW) function plus background(27) via:

$$S(\boldsymbol{q},\omega) = e^{-\langle u^2\rangle q^2/6}\left[A_0(\boldsymbol{q})\delta(\omega) + (1-A_0)\int_{-\infty}^{\infty}\frac{dt}{2\pi}e^{i\omega t - \left(\frac{|t|}{\tau}\right)^{\beta}}\right], \qquad \text{(S1)}$$

where $\langle u^2 \rangle$ is the mean-square displacement (MSD), $A_0(\boldsymbol{q})$ is the elastic incoherent structure factor (EISF), β is the stretching exponent and τ is the average relaxation time. The fits are illustrated in Fig. S2d. The resulting protein relaxation time, τ and the elastic incoherent structure factor (EISF) are plotted functions of q in Fig. S2 (e) and (f), respectively. τ has nearly no q dependence and is similar for substrate-free and camphor-bound CYP101, the averages being 37±4 ps and 40±6 ps, respectively, in good agreement with the $\chi''(q,\nu)$ data presented in Fig. 1b. For both samples, the stretching exponent β is ~0.6 and also q-independent. The q-independence of τ and β indicates that the average confined space for the motions of protein hydrogen atoms is smaller than $2\pi / q_{\max}$ (~ 3.3 Å). The EISF of substrate-free CYP101 is 4.3±0.4% lower than that of the camphor-bound form (Fig. S2f), confirming that the substrate-free form possesses larger-amplitude diffusive dynamics.

III.2 NMR Spectra and Data Fitting

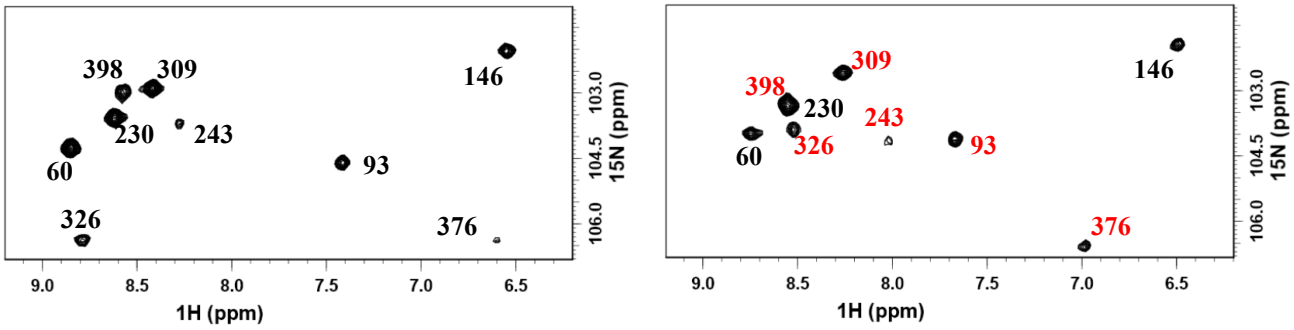

(a) (b)

Fig. S3 Comparison of corresponding selected regions of 2D ^{15}N-^{1}H TROSY-HSQC NMR spectra between (a) camphor-bound and (b) substrate-free CYP101. The resonances are labeled according to their sequential assignment. Resonances in red correspond to those that show the largest changes in chemical shifts and/or line-broadening between the two protein forms. Both spectra were acquired at 600 MHz and 300 K with protein sample conditions as described in Section I.1.

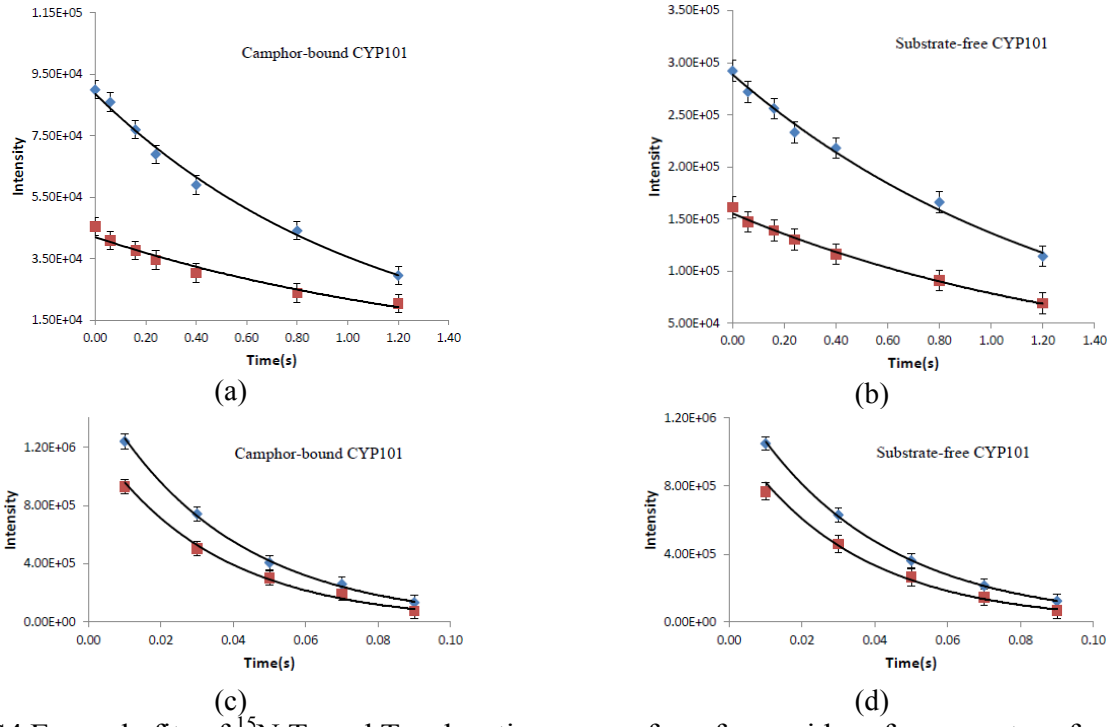

(a) (b)

(c) (d)

Fig. S4 Example fits of ^{15}N T_1 and T_2 relaxation curves for a few residues from spectra of camphor-bound and substrate-free CYP101 shown in Fig S3. The fits were determined as described in the text (*SI* I.3). (a) and (b) show T_1 fits to experimental data points for residues 309(blue) and 60(red), while (c) and (d) show T_2 fits to experimental data points for residues 309(blue) and 146(red).

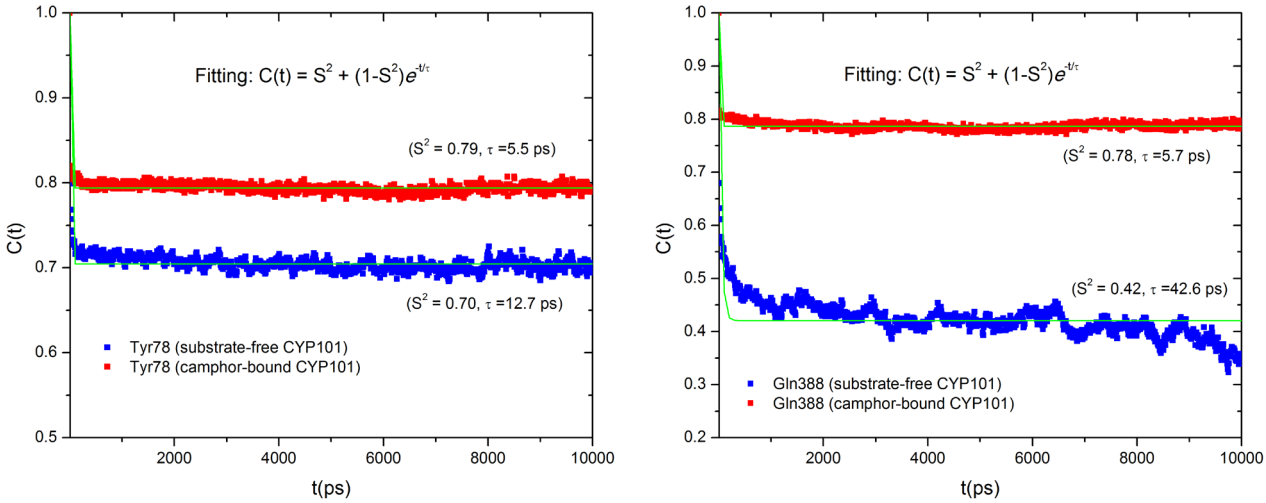

(a) (b)

Fig. S5 Example fits of the autocorrelation function of normalized *N*−*H* bond vectors for Tyr78 and Gln388 in substrate-free and camphor-bound CYP101 calculated from MD simulations.

III.3 Protein Dynamic Fluctuations from MD Simulation

Fig. S6a plots the ensemble-averaged channel opening, computed as the distance between the C_α atoms of Ser190 in the middle of the F/G loop and Pro89 at the N-terminus of the B′ helix, in substrate-free and camphor-bound CYP101 obtained from the MD simulations. To characterize the opening states of the channel in substrate-free CYP101, the displacements of the F and G helices relative to their positions in the "closed" 3L63 X-ray crystal structure are calculated by superimposing the C_α atoms of residues 295-405 (28) and plotted in Fig. S6b. Results show that the F helix moves closer to the B′ helix by ~1 Å, while the G helix moves closer by ~2 Å, but on average they are still ~3.5 Å and ~2.2 Å away from the positions in the "closed" conformation, respectively. This suggests that in substrate-free CYP101 the channel transitions from "open" towards the "partially open" conformation, but has not fully reached the position of the "partially open" conformation as defined in Ref. (28). Furthermore, the "closed" conformation is not accessible to the substrate-free protein.

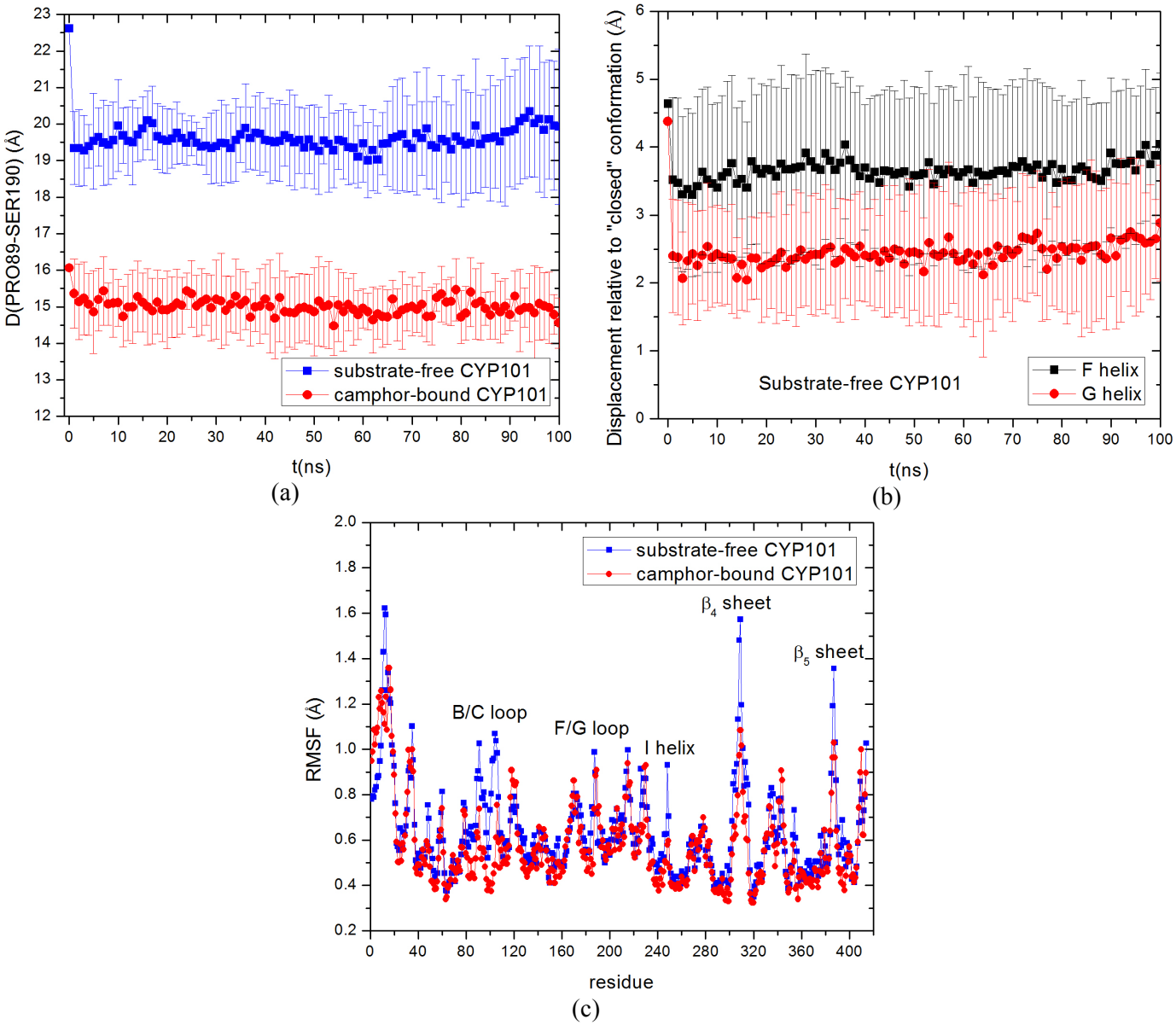

Fig. S6 (a) Plots of the ensemble-averaged channel opening (defined as the distance between the C_α atoms of Ser190 in the middle of the F/G loop and Pro89 at the N-terminus of the B' helix) calculated from MD simulations of substrate-free vs. camphor-bound CYP101. (b) The displacements of the F and G helices observed in the simulation of substrate-free CYP101 relative to their positions in the "closed" 3L63 X-ray crystal structure. (c) Comparison of RMSF of C_α atoms calculated from MD simulations of the two protein forms.

Fig. S6c plots the root mean square fluctuations (RMSF) of C_α atoms calculated from MD simulations of the two protein forms. Analysis of the plot suggests that substrate-free CYP101 is more dynamic than the camphor-bound form, especially in regions 78-105 (B/C loop containing

the B′ helix), 186-193 (F/G loop), 243-254 (the I helix kink near the active site), 305-313 (β_4 sheet) and 385-400 (β_5 sheet). MD simulations of CYP101 in aqueous solution indicate that similar protein regions exhibit increased dynamics in substrate-free CYP101 relative to the camphor-bound form as was observed in the hydrated powder simulations.

III.4 Orientation of Tyr96 in Protein Active Site

Fig. S7a shows that in substrate-free CYP101, the side chain of Tyr96 re-orients away from the active site occasionally forming a hydrogen bond with the carbonyl oxygen atom of Met184 from the F helix. Tyr96 exhibits much larger variations in the orientation of its side chain with significantly greater displacement of the hydroxyl oxygen atom from the position in the crystal structure in substrate-free CYP101 than in the camphor-bound form (Fig. S7b).

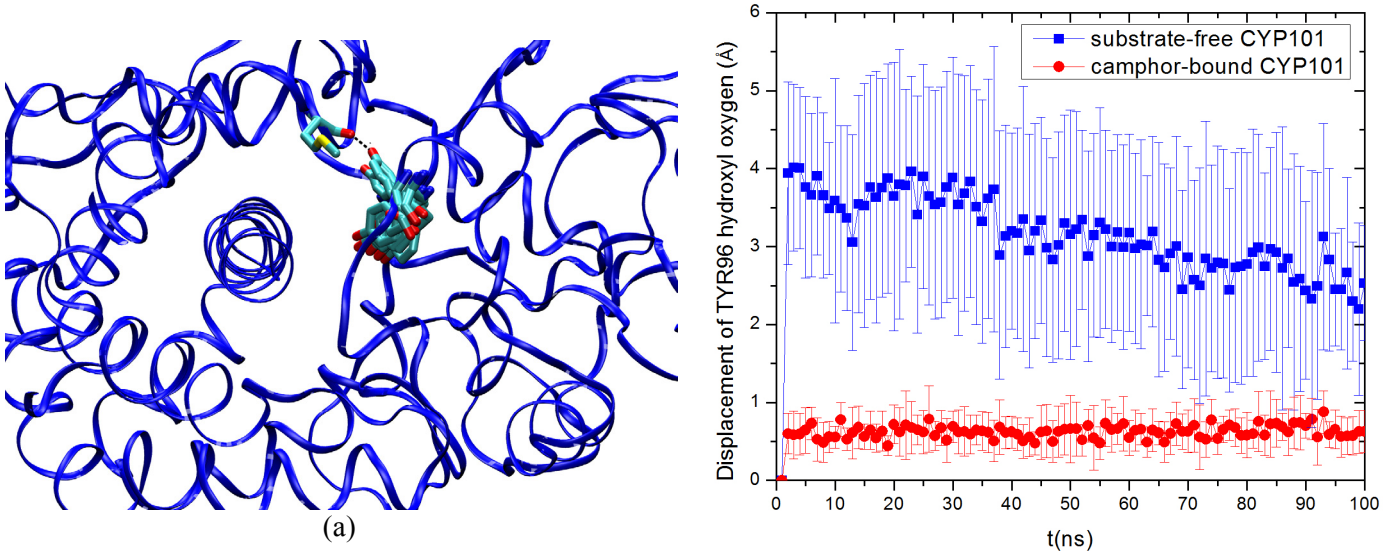

(a) (b)

Fig. S7 Orientations sampled by Tyr96 side chain: (a) depicting the hydrogen bond of hydroxyl group of Tyr96 formed with the carbonyl oxygen of Met184 in two of the eight proteins in the substrate-free CYP101 simulation and (b) the displacement of the hydroxyl oxygen atom in Tyr96 from its position in the crystal structure in the simulations of both protein forms.

III.5 Key Residue Interactions Surrounding the Channel Opening

Fig. S8 plots the distances of key salt-bridge, hydrogen-bonding and hydrophobic interactions with corresponding fluctuations surrounding the putative substrate access channel opening, i.e., Asp97-Lys197, Asp97-Tyr201 and Ala95-Phe193 connecting the B′ helix in the B/C loop and the G helix, Arg186-Asp182 and Arg186-Asp251 connecting the F helix, the F/G loop and the I helix, and Arg186-Val396 connecting the F/G loop and the β_5 sheet.

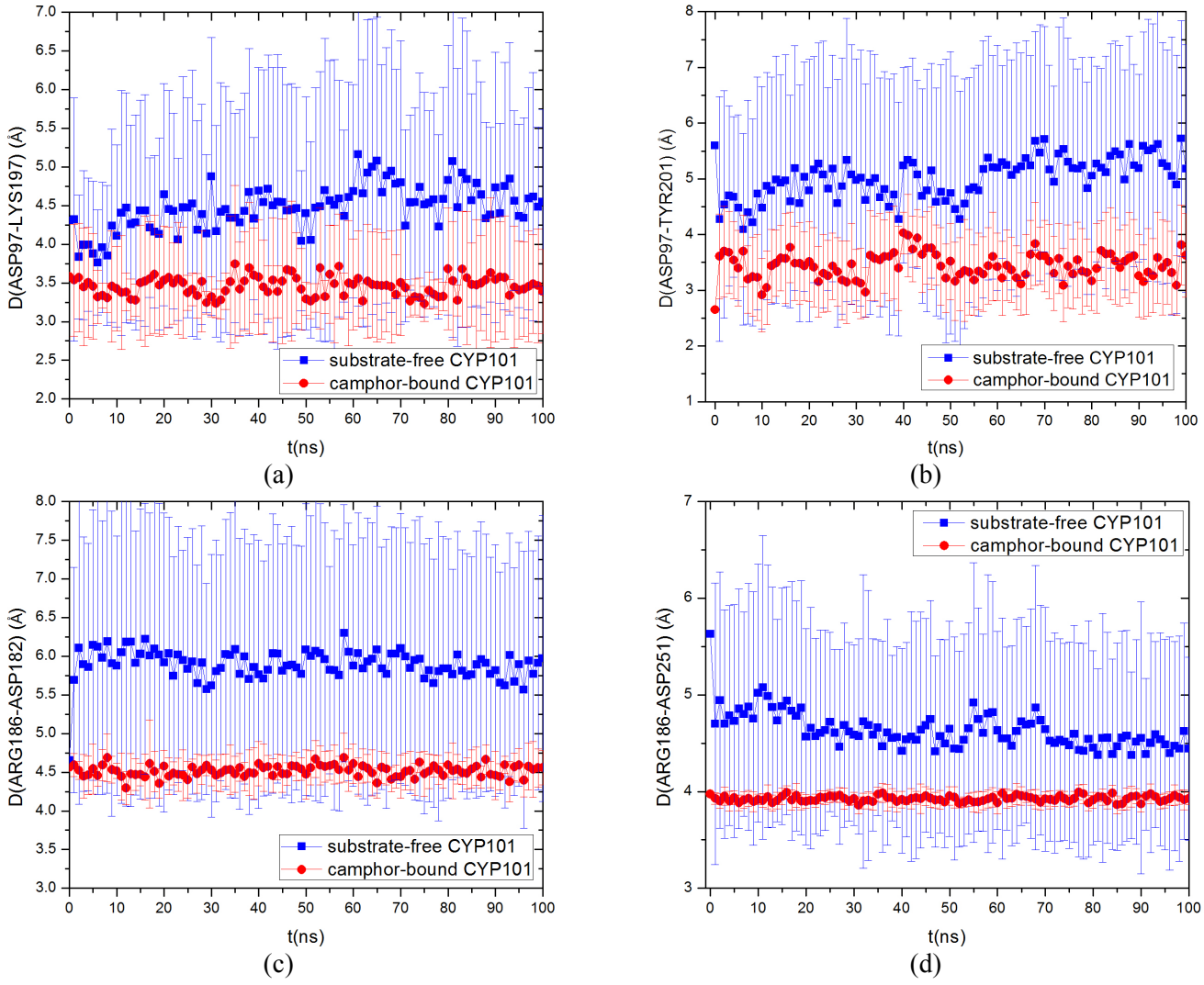

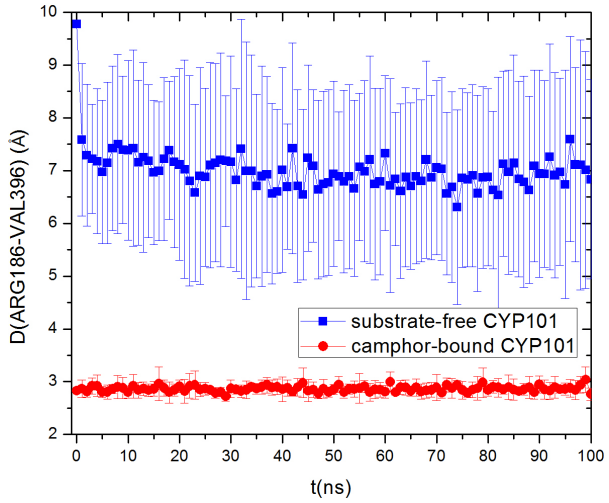

(e)

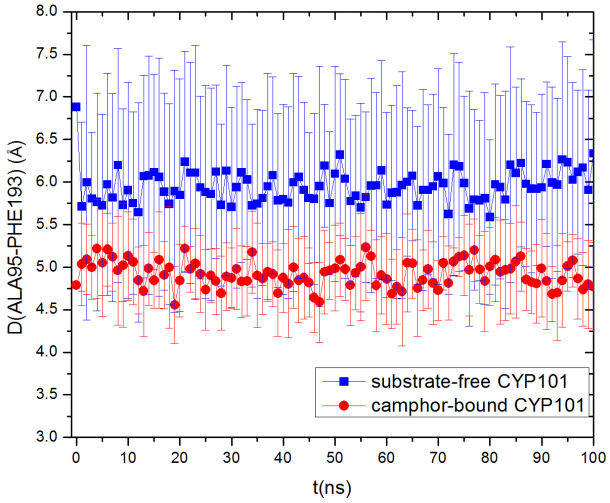

(f)

Fig. S8 Key residue interactions and their fluctuations in the putative substrate access site involving the F helix- F/G loop-G helix, the B′ helix and the β_5 sheet as depicted by the ensemble-averaged distances of eight proteins in CYP101 hydrated powder: (a) salt bridge Asp97-Lys197, (b) hydrogen bond Asp97 (side chain) – Tyr201 (-OH group), (c) Arg186-Asp182, (d) Arg186-Asp251, (e) hydrogen bond Arg186 (side chain) – Val396 (carbonyl oxygen), and (e) hydrophobic Ala95-Phe193.

III.6 Key Residue Interactions Connecting the B/C Loop and the β_4 sheet

Along the B/C loop, hydrogen bonding was found between residues Asp104-Ser83 and Phe97-Gln317, as well as Arg90 with Gly315 and Gln317. The residue distances are plotted in Figs. S9.

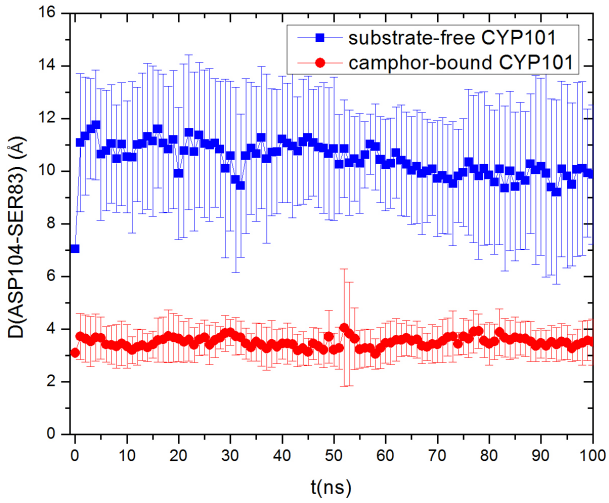

(a)

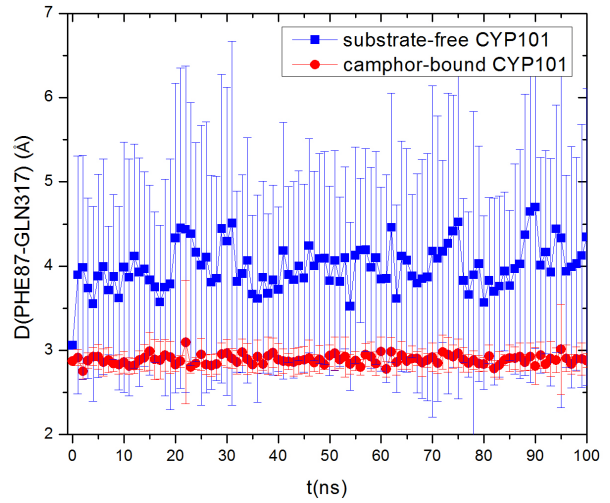

(b)

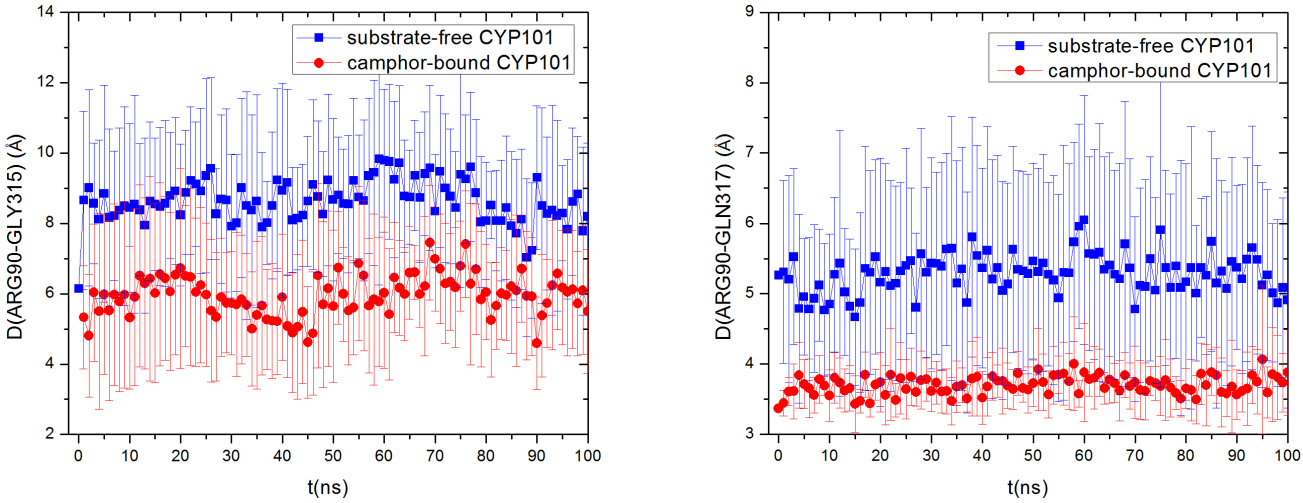

(c) (d)

Fig. S9 Key hydrogen-bonding interactions involved in the fluctuations of B/C loop and its interactions with the β_4 sheet as depicted by the ensemble-averaged distances of (a) Ser83 (side chain) – Asp104 (side chain), (b) Phe87 (carbonyl oxygen) – Gln317 (side chain), (c) Arg90 (side chain) – Gly315 (carbonyl oxygen), and (d) Arg90 (backbone nitrogen) – Gln317 (side chain).

References

1. Zhang, W., S. S. Pochapsky, T. C. Pochapsky, and N. U. Jain. 2008. Solution NMR Structure of Putidaredoxin-Cytochrome P450cam Complex via a Combined Residual Dipolar Coupling-Spin Labeling Approach Suggests a Role for Trp106 of Putidaredoxin in Complex Formation. J. Mol. Biol. 384:349-363.
2. Mamontov, E., and K. W. Herwig. 2011. A time-of-flight backscattering spectrometer at the Spallation Neutron Source, BASIS. journal article 82:085109.
3. Ehlers, G., A. A. Podlesnyak, J. L. Niedziela, E. B. Iverson, and P. E. Sokol. 2011. The new Cold Neutron Chopper Spectrometer at the Spallation Neutron Source - Design and Performance. journal article 82:085108.
4. Azuah, R. T., L. R. Kneller, Y. M. Qiu, P. L. W. Tregenna-Piggott, C. M. Brown, J. R. D. Copley, and R. M. Dimeo. 2009. DAVE: A Comprehensive Software Suite for the Reduction, Visualization, and Analysis of Low Energy Neutron Spectroscopic Data. J Res Natl Inst Stan 114:341-358.
5. Weigelt, J. 1998. Single scan, sensitivity- and gradient-enhanced TROSY for multidimensional NMR experiments (vol 120, pg 10778, 1998). J. Am. Chem. Soc. 120:12706-12706.
6. Yang, D., and L. E. Kay. 1999. Improved 1HN-detected triple resonance TROSY-based experiments. J. Biomol. NMR 13:3-10.
7. Delaglio, F., S. Grzesiek, G. W. Vuister, G. Zhu, J. Pfeifer, and A. Bax. 1995. NMRPipe: A multidimensional spectral processing system based on UNIX pipes. J. Biomol. NMR 6:277-293.
8. Farrow, N. A., R. Muhandiram, A. U. Singer, S. M. Pascal, C. M. Kay, G. Gish, S. E. Shoelson, T. Pawson, J. D. Forman-Kay, and L. E. Kay. 1994. Backbone dynamics of a free and phosphopeptide-complexed Src homology 2 domain studied by 15N NMR relaxation. Biochemistry 33:5984-6003.
9. Lakomek, N. A., J. Ying, and A. Bax. 2012. Measurement of (15)N relaxation rates in perdeuterated proteins by TROSY-based methods. J. Biomol. NMR 53:209-221.
10. Mandel, A. M., M. Akke, and A. G. Palmer, 3rd. 1995. Backbone dynamics of Escherichia coli ribonuclease HI: correlations with structure and function in an active enzyme. J Mol Biol 246:144-163.
11. Lee, Y. T., R. F. Wilson, I. Rupniewski, and D. B. Goodin. 2010. P450cam Visits an Open Conformation in the Absence of Substrate. Biochemistry 49:3412-3419.
12. Doster, W., S. Cusack, and W. Petry. 1990. Dynamic instability of liquidlike motions in a globular protein observed by inelastic neutron scattering. Phys Rev Lett 65:1080-1083.
13. Miao, Y., and J. Baudry. 2011. Active-Site Hydration and Water Diffusion in Cytochrome P450cam: A Highly Dynamic Process. Biophys. J. 101:1493-1503.
14. Yi, Z., Y. L. Miao, J. Baudry, N. Jain, and J. C. Smith. 2012. Derivation of Mean-Square Displacements for Protein Dynamics from Elastic Incoherent Neutron Scattering. Journal of Physical Chemistry B 116:5028-5036.
15. Zheng, J. J., A. Altun, and W. Thiel. 2007. Common system setup for the entire catalytic cycle of cytochrome P450(cam) in quantum mechanical/molecular mechanical studies. J. Comput. Chem. 28:2147-2158.
16. Poulos, T. L., B. C. Finzel, and A. J. Howard. 1986. Crystal-Structure of Substrate-Free Pseudomonas-Putida Cytochrome-P-450. Biochemistry 25:5314-5322.

17. Poulos, T. L., B. C. Finzel, and A. J. Howard. 1987. High-Resolution Crystal Structure of Cytochrome P450cam. J. Mol. Biol. 195:687-700.
18. Schlichting, I., J. Berendzen, K. Chu, A. M. Stock, S. A. Maves, D. E. Benson, B. M. Sweet, D. Ringe, G. A. Petsko, and S. G. Sligar. 2000. The catalytic pathway of cytochrome P450cam at atomic resolution. Science 287:1615-1622.
19. Yi, Z., Y. Miao, J. Y. Baudry, N. U. Jain, and J. C. Smith. 2012. Derivation of Mean-Square Displacements for Protein Dynamics from Elastic Incoherent Neutron Scattering. The Journal of Physical Chemistry B In press, DOI: 10.1021/jp2102868.
20. Jorgensen, W. L., J. Chandrasekhar, J. D. Madura, R. W. Impey, and M. L. Klein. 1983. Comparison of Simple Potential Functions for Simulating Liquid Water. J. Chem. Phys. 79:926-935.
21. Humphrey, W., A. Dalke, and K. Schulten. 1996. VMD: Visual molecular dynamics. Journal of Molecular Graphics 14:33-38.
22. Phillips, J. C., R. Braun, W. Wang, J. Gumbart, E. Tajkhorshid, E. Villa, C. Chipot, R. D. Skeel, L. Kale, and K. Schulten. 2005. Scalable molecular dynamics with NAMD. Journal of Computational Chemistry:1781-1802.
23. MacKerell, A. D., D. Bashford, M. Bellott, R. L. Dunbrack, J. D. Evanseck, M. J. Field, S. Fischer, J. Gao, H. Guo, S. Ha, D. Joseph-McCarthy, L. Kuchnir, K. Kuczera, F. T. K. Lau, C. Mattos, S. Michnick, T. Ngo, D. T. Nguyen, B. Prodhom, W. E. Reiher, B. Roux, M. Schlenkrich, J. C. Smith, R. Stote, J. Straub, M. Watanabe, J. Wiorkiewicz-Kuczera, D. Yin, and M. Karplus. 1998. All-Atom Empirical Potential for Molecular Modeling and Dynamics Studies of Proteins. J. Phys. Chem. B 102:3586-3616.
24. Schoneboom, J. C., H. Lin, N. Reuter, W. Thiel, S. Cohen, F. Ogliaro, and S. Shaik. 2002. The elusive oxidant species of cytochrome P450 enzymes: Characterization by combined quantum mechanical/molecular mechanical (QM/MM) calculations. J. Am. Chem. Soc. 124:8142-8151.
25. Essmann, U., L. Perera, M. L. Berkowitz, T. Darden, H. Lee, and L. G. Pedersen. 1995. A Smooth Particle Mesh Ewald Method. J. Chem. Phys. 103:8577-8593.
26. Ryckaert, J.-P., G. Ciccotti, and H. J. C. Berendsen. 1977. Numerical integration of the cartesian equations of motion of a system with constraints: molecular dynamics of n-alkanes. Journal of Computational Physics 23:327-341.
27. Williams, G., and D. C. Watts. 1970. Non-symmetrical dielectric relaxation behaviour arising from a simple empirical decay function. T Faraday Soc 66:80-85.
28. Lee, Y.-T., E. C. Glazer, R. F. Wilson, C. D. Stout, and D. B. Goodin. 2010. Three Clusters of Conformational States in P450cam Reveal a Multistep Pathway for Closing of the Substrate Access Channel. Biochemistry 50:693-703.